Research Square

Preprints are preliminary reports that have not undergone peer review.
They should not be considered conclusive, used to inform clinical practice,
or referenced by the media as validated information.

Seasonal and inter-seasonal soil moisture controls on coseismic shallow landsliding near the Cascadia Subduction Zone

Nicolas Mathews

nmathews@sitkascience.org

Sitka Sound Science Center https://orcid.org/0000-0002-4647-4039

Ben A. Leshchinsky

Oregon State University

Michael J. Olsen

Oregon State University

Adam M. Booth

Portland State University

Research Article

Keywords:

Posted Date: April 9th, 2026

DOI: https://doi.org/10.21203/rs.3.rs-9099855/v1

License: This work is licensed under a Creative Commons Attribution 4.0 International License.
Read Full License

Seasonal and inter-seasonal soil moisture controls on coseismic shallow landsliding near the Cascadia Subduction Zone

Nicolas W. Mathews[1], Ben A. Leshchinsky[2], Michael J. Olsen[3], Adam M. Booth[4]

[1] Sitka Sound Science Center, Sitka, AK, USA
[2] School of Civil and Construction Engineering, Oregon State University, Corvallis, OR, USA
[3] College of Forestry, Oregon State University, Corvallis, OR, USA
[4] Department of Geology, Portland State University, Portland, OR, USA

Corresponding author: Nicolas W. Mathews (nmathews@sitkascience.org)

ORCID IDs
Nicolas W. Mathews: 0000-0002-4647-4039
Ben A. Leshchinsky: 0000-0003-3890-1368
Michael J. Olsen: 0000-0002-2989-5309
Adam M. Booth: 0000-0002-7339-0594

Key Points

- We simulated the influence of soil moisture and seismicity on regional-scale shallow landslide initiation using a deterministic, three-dimensional slope stability model.
- Coseismic landslide response is highly sensitive to seasonal and inter-seasonal variations in soil moisture from antecedent rainfall.
- Spatial analyses of landslide density and yield acceleration highlighted regions in the Oregon Coast Range particularly susceptible to coseismic landsliding.

Plain Language Summary

Shaking from earthquakes commonly causes landslides which can threaten infrastructure and potentially cause more fatalities than the earthquake itself. Rainfall in the months leading up to an earthquake contributes to soil moisture and reduces soil strength, potentially worsening landslide activity during shaking. The relationship between soil moisture and landslides caused by earthquakes remains poorly understood and is difficult to understand from a limited number of historical earthquakes that caused widespread landsliding. To gain insight on this topic, we used computer simulations to evaluate a particularly landslide-prone region in western Oregon where major earthquakes pose a significant threat. Our calculations showed that landslides triggered during an earthquake are highly sensitive to both what time of year the earthquake occurs and the relative wetness of the year, with more landslides occurring when soils are wetter. We also created maps of landslide activity for a range of soil moisture conditions and earthquake magnitudes, highlighting specific locations of high landsliding potential during shaking.

Abstract

High levels of soil moisture tied to antecedent rainfall may predispose hillslopes to failure during earthquakes, but due to the infrequency of large earthquakes in a single region and lack of associated landslide inventories with well-characterized soil moisture data, characterizing the influence of soil moisture on coseismic shallow landsliding remains challenging. We used RegionGrow3D – a three-dimensional slope stability model that simulates landslide initiation on a regional scale – to simulate coseismic shallow landslides in a region of the Oregon Coast Range, USA, near the Cascadia Subduction Zone. Using this framework, we quantified the influence of seasonally dependent soil moisture, seismic acceleration, and soil shear strength uncertainty on landslide density, landslide scaling relationships, and spatial distributions of yield accelerations. We also demonstrated that, in some cases, seasonality and soil moisture may be a stronger control on coseismic landsliding than peak ground accelerations.

1. Introduction

Landslides frequently accompany earthquakes, contributing to mass wasting and losses of life and infrastructure (Dadson et al., 2004; Froude & Petley, 2018; Keefer, 1984, 2002; Parker et al., 2011; Schuster & Highland, 2001). Over 3,400 coseismic landslides were inventoried on Honshu, Japan following the 2011 Tohoku Earthquake (M_w9.0) and over 25,000 landslides were documented after the 2015 Gorkha earthquake (M_w7.8) in Nepal (Roback et al., 2018; Wartman et al., 2013). The 2008 Wenchuan earthquake (M_w7.9) in China triggered more than 60,000 landslides, which caused about 80% of the total earthquake fatalities (Huang & Fan, 2013). Coseismic landslides can also hinder post-disaster recovery (Bayer, 2017; Olsen et al., 2015; Sharifi-Mood, 2017).

Elevated soil moisture from antecedent rainfall reduces effective stress in soils, predisposing hillslopes to failure (Lu & Likos, 2006; Terzaghi, 1950; Wieczorek, 1996) and potentially exacerbating landslide activity caused by earthquakes. Many large earthquakes occur in regions with variations in soil moisture both throughout the year and from season to season, making soil moisture a paramount consideration in coseismic landslide hazard assessment. However, there are few studies characterizing the relationship between soil moisture, seismicity, and shallow landslide initiation. (Martino et al., 2022) found that rainfall preceding the 2018 earthquake in Montecilfone, Italy (M_w5.1) decreased hillslope stability at the catchment-scale, consequently increasing coseismic landslide activity. Some have also speculated that heavy rainfall before the 2018 earthquake in Hokkaido, Japan (M_w6.6) caused anomalously high levels of landsliding (Petley, 2018; Wang et al., 2019; Zhang et al., 2019). However, a comprehensive understanding of the relationship between soil moisture and coseismic landslide initiation remains elusive due to the relative infrequency of large earthquakes in a single region and lack of associated landslide inventories with well-characterized soil moisture data.

Where coseismic inventory data are sparse, deterministic models may be used to simulate coseismic landslide initiation tied to a wide range of seismic and hydrological conditions (e.g.,(Hess et al., 2017; Zhang & Wang, 2019). However, quantifying erosional patterns for landslides via

modeling, such as magnitude-frequency and area-volume relationships (Guzzetti et al., 2009; Malamud et al., 2004), requires a model that can estimate realistic coseismic landslide geometries on a broad regional scale. To address this, we parameterized RegionGrow3D (RG3D; Mathews et al., 2024; Mathews & Leshchinsky, 2024) – a three-dimensional (3D), physics-based, hydromechanical model of landslide initiation developed for regional-scale simulations – to account for ground accelerations caused by earthquakes.

Yield acceleration, k_y, describes the threshold base acceleration required to overcome shear resistance and initiate landsliding (Jibson, 2011; Kramer, 1996; Makdisi & Seed, 1978; Sarma, 1973), which is useful for characterizing the coseismic landslide susceptibility of hillslopes. Mathews et al. (2019) considered the spatiotemporal development of yield accelerations for individual hillslopes and Martino et al. (2022) assessed rainfall-induced changes in yield accelerations at the catchment scale using a one-dimensional slope stability model, but to our knowledge, no study has used a deterministic model to assess yield accelerations for discrete, 3D landslide sources across a broad landscape, for both seasonal and inter-seasonal variations in soil moisture.

We used RG3D to assess the stability and 3D geometry of shallow landslides for three earthquake scenarios and a range of antecedent soil moisture conditions in western Oregon, a particularly landslide-prone region of the Pacific Northwest in close proximity to the Cascadia Subduction Zone (CSZ). This region experiences a wide variety of earthquake types, including crustal (Madin et al., 1993; Wiley et al., 1993) and intraplate earthquakes (Madin & Mabey, 1996). However, because there are no existing records of shallow landslides triggered by the CSZ, which has a history of producing powerful megathrust earthquakes (Goldfinger et al., 2012), we focused on modeling CSZ-triggered shallow landslides for three scenarios: a M_w8.1, M_w8.4, and M_w9.0 megathrust earthquake. We quantified the regional-scale influence of antecedent soil moisture and seismic acceleration on (1) landslide density, (2) landslide scaling relationships, (3) seasonal landsliding throughout the year, and (4) spatial distributions of yield accelerations.

2. Methodology and Parameterization

2.1. Pseudostatic Extension of the RegionGrow3D Model

We computed 3D landslide initiation geometries using RG3D, modified in this study to account for seismic acceleration using the pseudostatic approach (Jibson, 2011; Kramer, 1996). RG3D identifies unstable cells within a digital elevation model (DEM) which are then grouped into discrete clusters and grown downslope to achieve force equilibrium (Figure S1). RG3D considers forces acting on the boundary of the landslide, which we also modified to account for coseismic acceleration (Section 1.1 in supporting information [SI]). Incorporating the pseudostatic approach yielded the following equation for the intercolumn resultant force, Q, for each soil column:

$$Q = N \sin\beta - [c'A + (N - uA)\tan\phi'] \cos\beta + k_h W \quad (1)$$

where c' is mineral cohesion, A is the column basal slip surface area, u is porewater pressure (when u is positive) or suction stress (when u is negative) at the base of the column, ϕ' is the effective

friction angle. In this study, c' is equal to 0 kPa, as apparent cohesion stems from moisture-dependent processes (Lu & Likos, 2013) better captured by the hydromechanical model and we assume the granular source material for shallow landslides demonstrates negligible mineral cohesion. The sensitivity of landslide initiation to mineral cohesion is quantified for this study area in the SI of Mathews et al. (2024). k_h is the horizontal pseudostatic coefficient:

$$k_h = PGA/g \quad (2)$$

where PGA is horizontal peak ground acceleration and g is gravitational acceleration. We assumed that seismic acceleration acts in the direction of sliding and omitted vertical acceleration, which tends to have a negligible effect on slope stability (Kramer, 1996). The selection of k_h as a representation for the transient and dynamic effects of seismic shaking is notoriously challenging. Because bodies of soil are flexible and the PGA only manifests for a short time period during an earthquake, k_h is often scaled using a factor between 0 and 1. Since this study is focused on the relative degree of landsliding between earthquake magnitudes, as opposed to precise characterization of landslide activity for a given earthquake, we assumed a scaling factor of 1. This is higher than usual but may partially account for the long duration of megathrust earthquakes while also eliminating the need to choose an ambiguous scaling factor for the calculation of k_h. We do not consider potential increases in pore water pressure during shaking or dilatancy/contraction that may increase or decrease resisting forces at large deformation. We also do not consider the destabilization of surrounding material following landslide evacuation, but a sensitivity study assessing this phenomenon may be found in the SI of Mathews et al. (2024).

2.2. Soil Shear Strength, Landslide Susceptibility Maps, and Discrete Landslides

We parameterized RG3D with a distribution of friction angles, ϕ', and their associated probabilities (Figure 1a), originally back-calculated by Mathews et al. (2024) using a landslide inventory from the Gales Creek quadrangle, Oregon (Figure 2b; Burns et al., 2012), using 3D limit equilibrium (Bunn et al., 2020a, 2020b). This distribution of ϕ' enabled the assessment of landslide susceptibility as described in Mathews et al. (2024). A susceptibility threshold, T, which directly corresponds with ϕ' (Figure 1b), was used to create a distribution of discrete landslides from susceptibility maps (Figure S2; Mathews et al., 2024). For example, for T = 80%, we only considered pixels with 80% susceptibility or greater as landslide pixels and then regrouped those pixels into discrete landslides. In doing this, we are assigning the 80th percentile of shear strength, as determined from the landslide inventory, as the minimum shear strength in the landscape (Figure S2c). As T increases, the resulting landslide distribution reflects higher soil shear strength conditions.

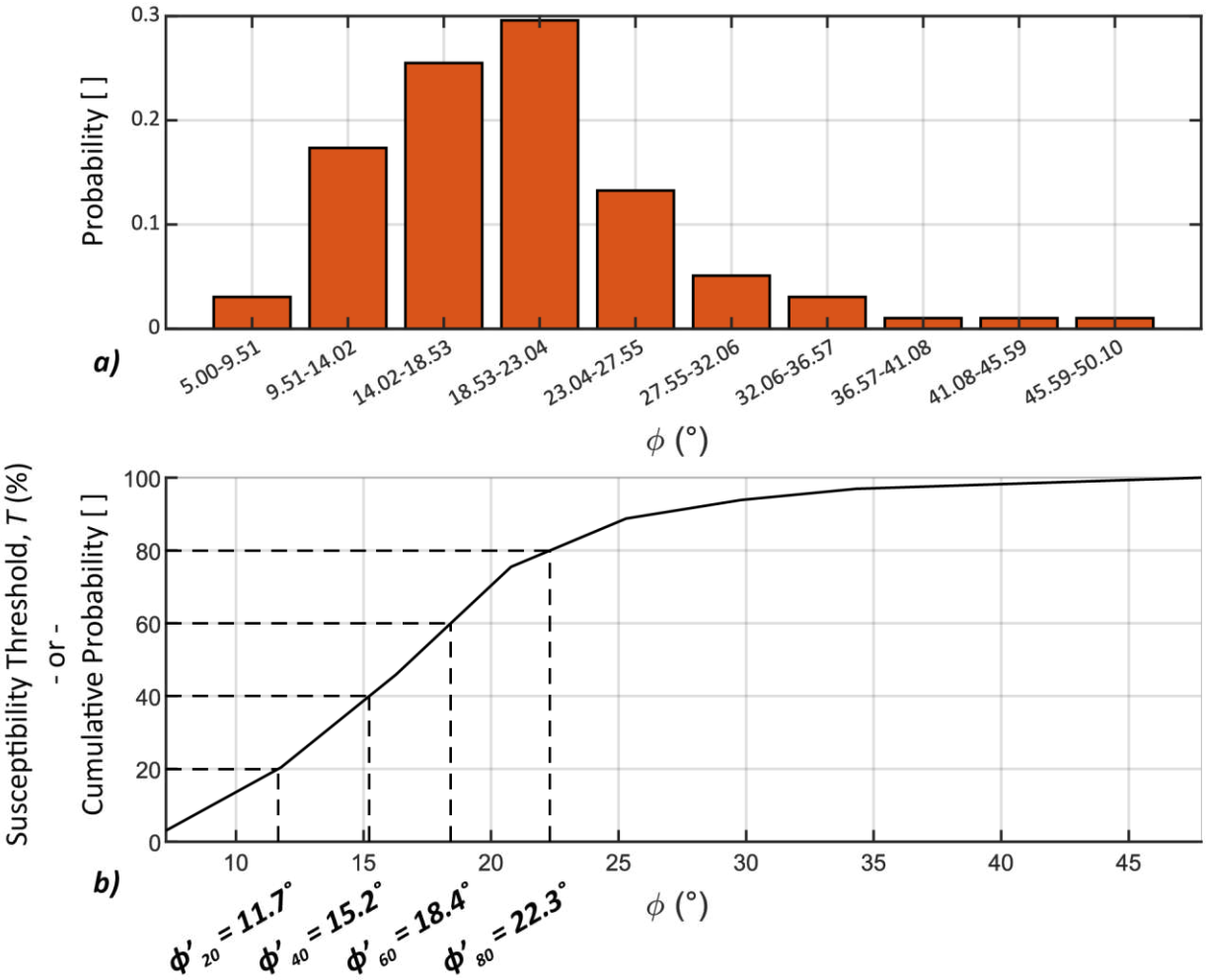


Figure 1: Back-calculated shear strength for study area: a) Friction angle, ϕ', and associated probabilities (after Mathews et al., 2024); b) relationship between ϕ' and susceptibility threshold, T (cumulative probability of ϕ'). Friction angles are back calculated from the Gales Creek landslide inventory as described in Mathews et al. (2024).

2.3. Soil Depth and Hydromechanical Parameterization

We assumed that shallow landslides fail at the interface of bedrock and soil, and computed soil depth using a nonlinear hillslope evolution model calibrated to the Oregon Coast Range (Roering, 2008), parameterized as described in Mathews et al. (2024). We used a hydromechanical model, parameterized with antecedent soil moisture and van Genuchten (1980) parameters from a lookup table based on the ROSETTA pedotransfer model (Schaap et al., 2001), to compute a vertical profile of volumetric water content, θ (m^3/m^3), for each soil column and associated suction stress or pore water pressure at the failure interface (Lehmann et al., 2019; Leshchinsky et al., 2021; Mathews et al., 2024). We categorized the DEM using soil textural classes (Figure 2b) that each demonstrate a different hydrological response, ultimately influencing effective stress conditions (Mathews et al.,

2024). We did not consider rotational landslides failing in rock in this study, which are less sensitive to near surface variations in soil moisture.

To evaluate slope stability across seasonal and inter-seasonal moisture variability, we compute antecedent soil moisture for relatively dry, mean, and wet years, for each month of the water year. We use 9-km, root-zone (1-m deep) soil moisture time series from the Soil Moisture Active Passive (SMAP) satellite mission (Reichle et al., 2019). For each grid cell, we obtained time histories of θ through the Application for Extracting and Exploring Analysis Ready Samples (AppEEARS) interface (Quenzer & Friesz, 2015) for the period spanning March 31, 2015 to August 28, 2020 (3-hour temporal resolution). We computed daily means, $\bar{\theta}$, and standard deviations, σ, across all years for each calendar day, and "dry", "mean", and "wet" conditions were defined as $\bar{\theta} - \sigma$, $\bar{\theta}$, and $\bar{\theta} + \sigma$, respectively. We then computed monthly averages for each grid cell and condition, producing 36 unique spatial distributions of θ (dry/mean/wet for each month of the year; Figure 2c–d). A bias correction of 0.055 m^3/m^3 was applied to account for known SMAP overestimation in mountainous forested terrain (Reichle et al., 2017). These distributions were used as inputs to the hydromechanical model to compute pore-pressure and effective-stress conditions.

2.4. Cascadia Subduction Zone Rupture Scenarios and Peak Ground Acceleration

Spatial distributions of site-specific, horizontal PGA for three CSZ rupture scenarios – M_w8.1, M_w8.4, and M_w9.0 - are the seismic inputs for RG3D (Figure 2e-f; Figure S4). Sharifi-Mood (2017) computed these distributions by applying site-amplification equations (Boore & Atkinson, 2008) to synthetic distributions of bedrock PGA, generated using the *ShakeMap* software (Worden et al., 2018). These three CSZ scenarios all rupture the same southern area of the fault (orange shading in Figure 2a), but as magnitude increases, the total rupture area extends northward (Figure 2a; Sharifi-Mood, 2017). Thus, PGA throughout the study area depends on proximity to the fault and rupture geometry and would likely differ for study areas in other locations.

2.5. Spatial Distribution of Yield Accelerations

To create spatial distributions of yield accelerations, we applied uniform PGA values (in 0.025 g increments) to the DEM and computed susceptibility for each increment. We then applied a susceptibility threshold to each map to identify discrete landslides. For each distribution, we assigned the corresponding PGA value to all landslides and compiled these values into a single map, where each assigned yield acceleration represents the minimum PGA required to initiate failure. We repeated this process for dry, mean, and wet conditions, producing yield-acceleration maps for a range of antecedent moisture states and for any chosen susceptibility threshold.

2.6. Study Area

We applied these methods to the same study area as Mathews et al. (2024): a 6-m-resolution DEM of a 1,068 km^2 region in the Oregon Coast Range with widespread landslide activity and significant seismic hazard associated with the CSZ (Figure 2a–b). The DEM is derived from

topographic light detection and ranging (lidar) data from the Oregon Lidar Consortium (Oregon Department of Geology and Mineral Industries, 2022). The study area includes marine sedimentary rocks, basalts, and localized alluvial deposits in the western region; predominantly basaltic and marine sedimentary units in the central and eastern regions; extensive Missoula flood deposits east of the Coast Range; and isolated exposures of the landslide-prone early Tertiary Tyee Formation in the southwest (Mathews et al., 2024; Smith & Roe, 2015).

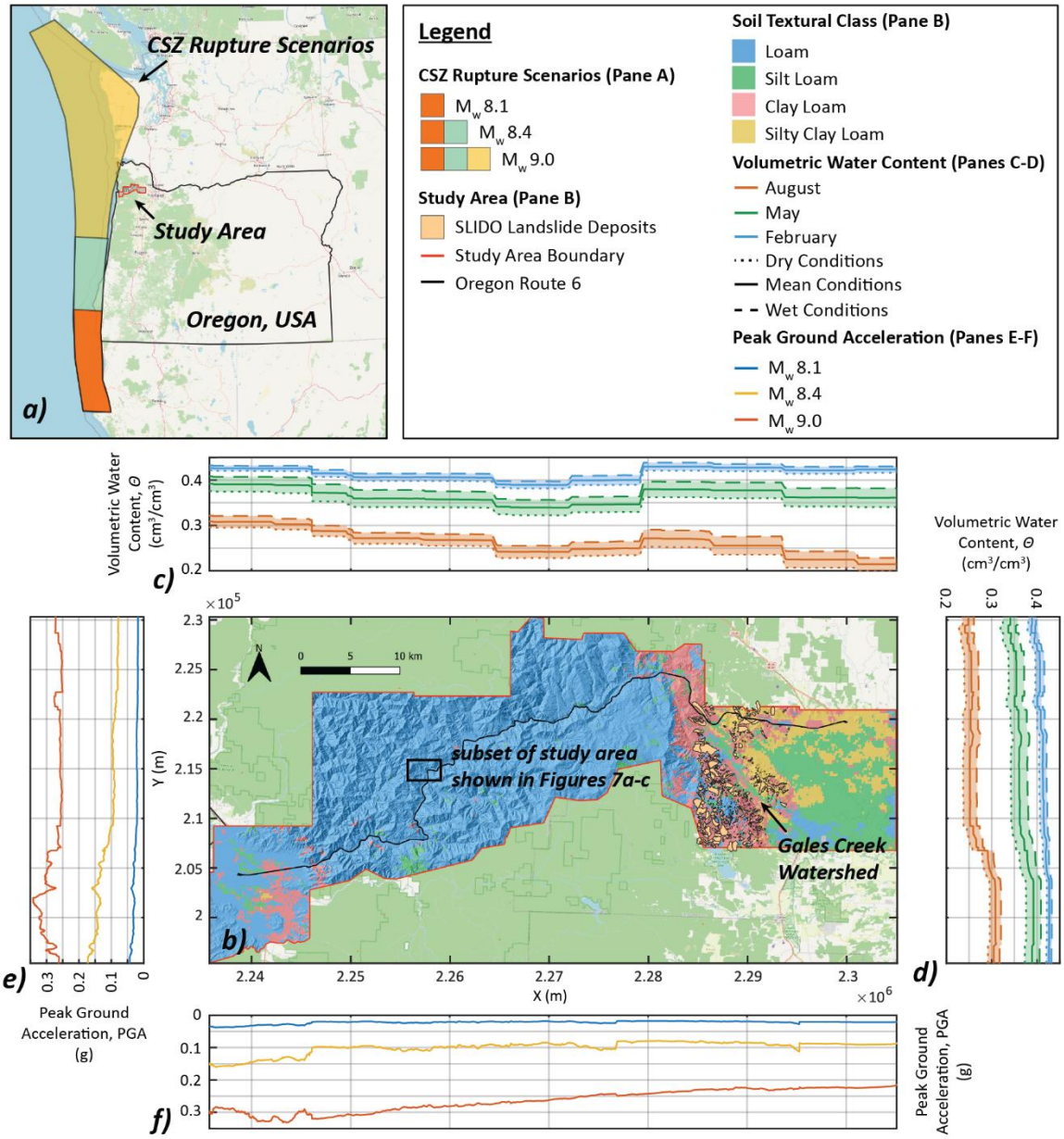


Figure 2: (a) Location of study area and Cascadia Subduction Zone rupture scenarios; (b) Map of study area (after Mathews et al., 2024). Distributions of mean volumetric water content for select months (February - blue, May - green, August - orange) and inter-seasonal variations in soil

moisture (dry, mean, wet) for each (c) column and (d) row. Distributions of mean peak ground acceleration (M_w9.0 - orange, M_w8.4 - yellow, M_w8.1 – blue) for each (e) row and (f) column.

3. Results

3.1. Landslide Density: Influence of Seasonality and Spatial Distribution

We computed coseismic landslide area density (LAD) for each month of the water year (October 1 to September 30), accounting for inter-seasonal moisture -- dry, mean, and wet conditions -- and three CSZ rupture scenarios ($T = 50\%$; $\phi' = 16.9°$; Figure 3). LAD is the total area of simulated landsliding normalized by the total DEM area. Modeled LAD is highest in wetter months (e.g., January and February) and low or negligible in drier months (e.g., August and September), with a more rapid increase during the wetting season (September to January) than the decline during drying season (February to August). For a given earthquake magnitude, LAD increases under wetter conditions, and for a given moisture state, LAD increases with earthquake magnitude; however, LAD reflects a strong trade-off between shaking and antecedent moisture, such that larger earthquakes do not necessarily produce greater landslide area.

The sensitivity of LAD to earthquake magnitude and inter-seasonal moisture decreases during winter months, when persistently wet conditions have already reduced effective stress across the landscape. During these months, differences between dry, mean, and wet years become muted, indicating that typical seasonal rainfall plays a primary role in preconditioning the landscape for coseismic landsliding.

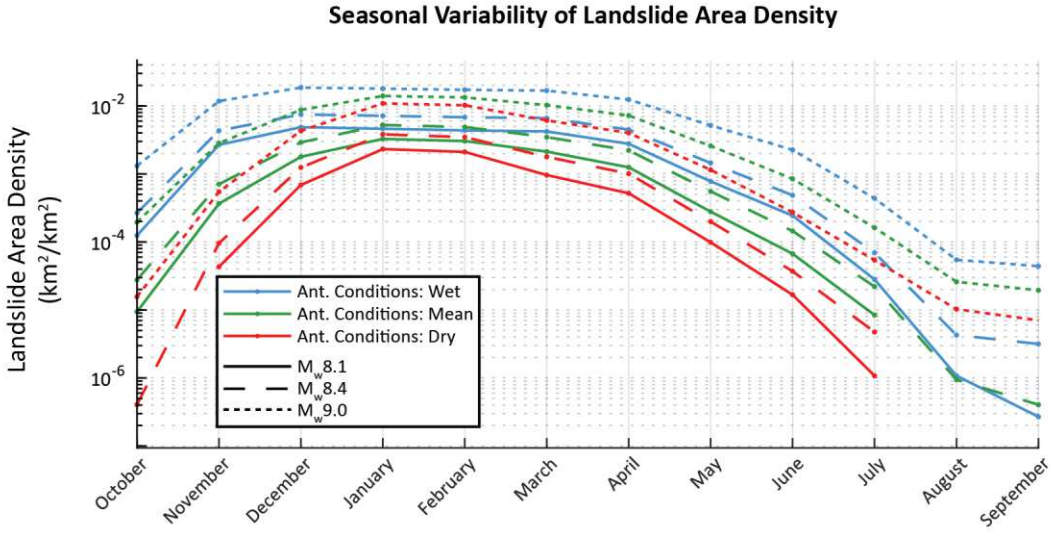


Figure 3: Landslide area density (LAD), computed using $T = 50\%$ ($\phi' = 16.9°$), for each month of the water year, a range of earthquake scenarios (M_w8.1, M_w8.4, and M_w9.0), and different degrees of relative inter-seasonal wetness (dry, mean, and wet conditions).

We examined spatial patterns of LAD and landslide density (LD) for a M_w9.0 earthquake during February ($T = 50\%$; $\phi' = 16.9°$; Figure 4). We define LD as the number of landslides per 240-m grid cell (0.058 km^2), a resolution selected to capture spatial clustering. Values shown in Figure 4b-c and Figure 4d-e correspond to each row and column, respectively. For all inter-seasonal moisture conditions, LAD is highest in the western Coastal Mountains, where soil moisture is relatively high (Figure 2c) and PGA is highest due to proximity to the CSZ (Figure 2a,f). LAD is also elevated in northern and southern portions of the study area and in a localized region west of the Gales Creek Watershed (Figure 2b). LAD and LD increase with wetter inter-seasonal moisture, especially in the western Coastal Mountains, indicating that landslides are both more widespread and numerous. Maps of LAD for dry, mean, and wet conditions are shown in Figure S4.

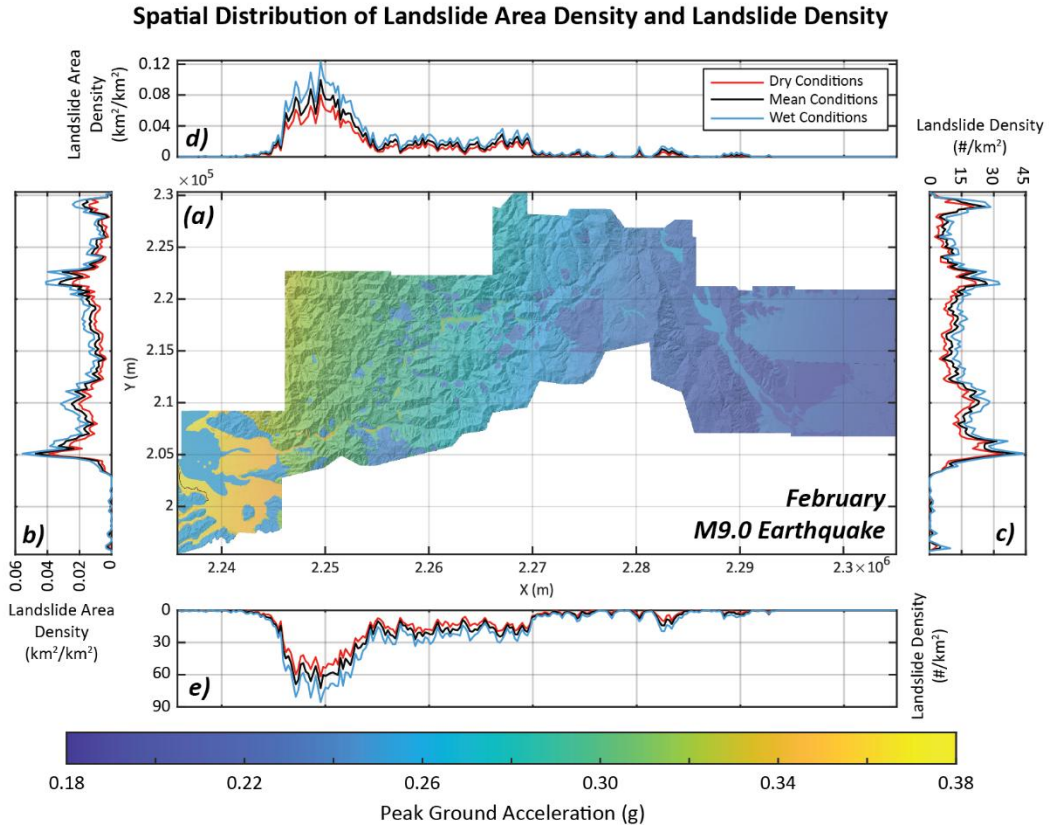


Figure 4: (a) Map of peak ground acceleration for a M_w9.0 earthquake; (b) LAD for each row; (c) Landslide density (LD) for each row; (d) LAD for each column; (e) LD for each column. LAD and LD were computed using $T = 50\%$ ($\phi' = 16.9°$).

3.2. Landslide Scaling Relationships

Landslide scaling relationships relate landslide characteristics for understanding erosional processes at the landscape scale, such as area, volume, and frequency. We quantified the sensitivity of these relationships to CSZ rupture scenarios and inter-seasonal variations in soil

moisture using frequency density (FD) and probability density (PD; February, $T = 50\%$; $\phi' = 16.9°$; Figure 5). FD is the number of landslides across bins of landslide area, normalized by that area range, and PD is FD normalized by the total number of landslides (Malamud et al., 2004). FD increases with both earthquake magnitude and wetter antecedent conditions, indicating more numerous shallow landslides for a broad range of areas (Figure 5a-c). Similar FD curves can result from different combinations of earthquake magnitude and moisture, depending on preceding antecedent moisture (e.g., M_w8.4 earthquake during wet conditions versus M_w9.0 earthquake during dry conditions).

Across all magnitudes and inter-seasonal moisture states, PD remains relatively invariant over most landslide areas (Figure 5d-f). However, wetter conditions slightly increase the probability of larger-area landslides, and higher magnitudes extend PD curves toward larger maximum landslide areas. For a wide range of landslide areas, modeled PD curves align well with curves derived from event-based landslide inventories (Malamud et al., 2004). The sensitivity of FD and PD to shear strength (T) is shown in Figure S5.

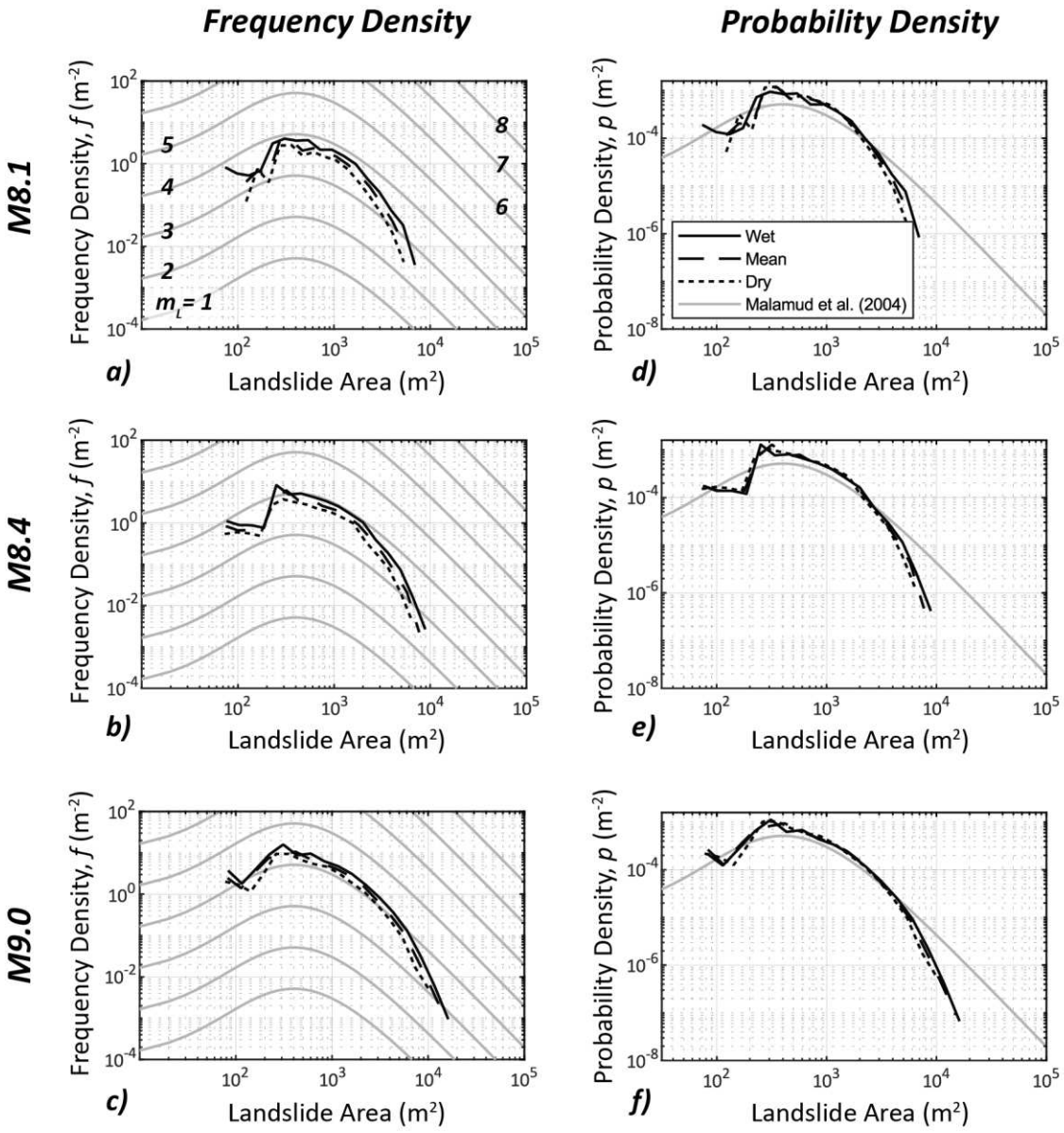


Figure 5: Landslide area scaling relationships (February; $T = 50\%$; $\phi' = 16.9°$): (a) Frequency density (FD; M_w8.1); (b) FD (M_w8.4); (c) FD (M_w9.0); (d) Probability density (PD; M_w8.1); (e) PD (M_w8.4); (f) PD (M_w9.0). The gray curves in parts (a), (b), and (c) represent the magnitude of a landslide event, based on the total number of landslides (Malamud et al., 2004).

3.3. Parametric Landslide Area Density for Uniform Moisture and Seismic Forcing

To generalize the combined influence of soil moisture, seismicity, and shear strength uncertainty, we computed LAD for uniform values of θ, PGA, and T and uniformly-applied values of and PGA (Figure 6). LAD varies considerably across the parameter space and similar LAD values can result from multiple combinations of θ, PGA, and T. As shear strength decreases (i.e., T), comparable LAD values occur at lower θ and PGA. This parametric framework enables LAD

estimation where spatial distributions of moisture or seismic acceleration are unknown and provides a basis for calibration against landslide inventories from past earthquakes (e.g., Kaikoura, 2016; Massey et al., 2021; Hokkaido, 2018; Wang et al., 2019). With prior knowledge of antecedent moisture conditions during these events, T could be modified to best match their LAD values, potentially providing insight into the bounds of ϕ' for a given region.

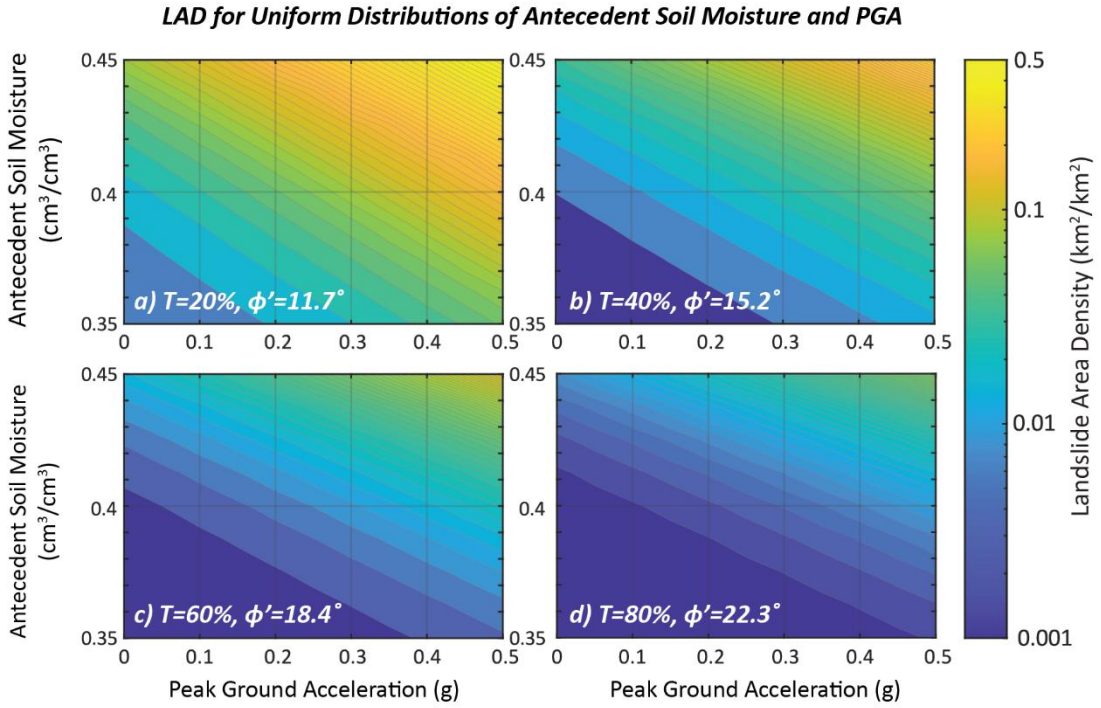


Figure 6: Landslide area density (LAD) for uniform distributions of volumetric water content and uniform distribution of peak ground acceleration (PGA) in February: (a) $T = 20\%$ ($\phi' = 11.7°$); (b) $T = 40\%$ ($\phi' = 15.2°$); (c) $T = 60\%$ ($\phi' = 18.4°$); (d) $T = 80\%$ ($\phi' = 22.3°$).

3.4. Spatial Distributions of Yield Acceleration

We computed yield acceleration, k_y, for February under dry, mean, and wet inter-seasonal conditions ($T = 50\%$; $\phi' = 16.9°$; Figure 8). For dry conditions, $k_y < 0.2g$ is limited to steep slopes, whereas wetter conditions reduce k_y across much of the landscape, indicating lower accelerations required to cause failure. Cumulative distributions of k_y for the entire study area highlight the sensitivity of yield acceleration to T and inter-seasonal moisture (Figure 8d); probabilities do not sum to unity because only failed cells are included.

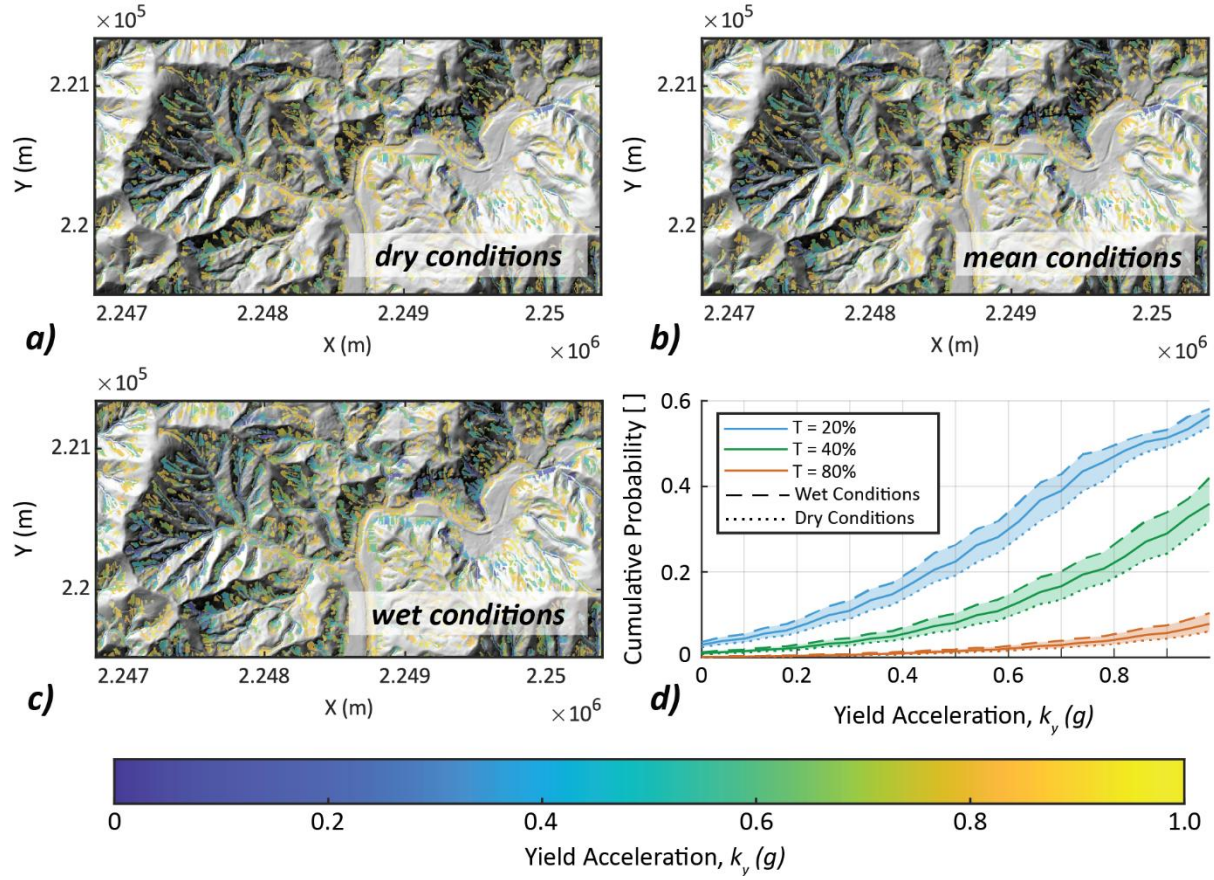


Figure 7: Yield accelerations for a subset of the study area in February for: (a) dry conditions ($T = 50\%$); (b) mean conditions ($T = 50\%$); (c) wet conditions ($T = 50\%$). Cumulative probability of yield accelerations for the entire study area ($T = 20\%$, $\phi' = 11.7°$; $T = 40\%$, $\phi' = 15.2°$; $T = 80\%$, $\phi' = 22.3°$) shown in part (d). A bounding box for this subset of the study area is shown in Figure 2b.

4. Discussion

4.1. Hydrology as a Control on Coseismic Landsliding

Our results demonstrate that coseismic landslide response in the Oregon Coast Range depends strongly on both seasonal timing (i.e., the month in which an earthquake occurs) and inter-seasonal wetness (i.e., whether antecedent conditions reflect a dry, average, or wet year). Elevated antecedent rainfall increases soil saturation and reduces effective stress, which increases LAD and lowers yield accelerations, indicating higher coseismic landslide susceptibility across the landscape. As a result, similar Cascadia Subduction Zone rupture scenarios may produce markedly different landslide outcomes depending on whether it occurs during the summer, the autumn wetting season, or periods of peak winter saturation.

The reduced sensitivity of LAD to earthquake magnitude during winter further indicates that hydrologic conditions exert a stronger control on landslide response when soils are wet. Although seismic shaking ultimately triggers coseismic landslides, earthquake magnitude plays a secondary role once effective stress has already been substantially reduced by antecedent moisture. While our model does not account for excess pore water pressure generation during cyclic loading, this process also requires saturated pore spaces to develop, reinforcing the conclusion that hydrologic preconditioning is a primary control on coseismic landslide susceptibility.

4.2. Implications for Landslide Susceptibility and Risk near the Cascadia Subduction Zone

These findings highlight the importance of seasonal moisture, inter-seasonal moisture, and the spatial distribution of moisture as key factors for assessing hazard and risk from coseismic landslides in the Oregon Coast Range. The coincidence of elevated soil moisture from abundant rainfall and high PGA from proximity to the CSZ in the western Coast Range highlights a region of particularly high hazard and risk from coseismic landslides, especially if a CSZ rupture were to occur in the middle of winter on a particularly rainy year. This work emphasizes that incorporating seasonal soil moisture data into seismic hazard assessments could help identify high risk locations for which to prioritize response readiness. Further, expressing landslide susceptibility as yield acceleration provides a direct link to triggering accelerations from earthquakes for a range of hydrological conditions, making planning around specific earthquake scenarios easier.

4.3. Scaling Relationships: Dependence on Antecedent Moisture and Earthquake Magnitude

Variations in frequency density between triggering scenarios shows that increased earthquake magnitude and wetness make landslides more abundant; however, the relative invariance in probability density curves indicates that these factors are not the sole primary control on the distribution of landslide sizes, and reinforces findings that characteristic landslide size is largely controlled by source material strength and topographic relief (Medwedeff et al., 2020).

4.4. Model Limitations and Assumptions

The RegionGrow3D (RG3D) model, adapted here for seismic slope stability assessment, does not simulate excess pore water pressure generation during cyclic loading. We parametrized this version of RG3D using the pseudostatic approach and scaled PGA, which captures shaking intensity but does not represent earthquake duration or the directionality of shaking. As implemented, RG3D simulates shallow landslide initiation and does not simulate deeper rotational landslides in bedrock.

Although we simulated a range of uniform shear strength scenarios to represent parameter uncertainty, the spatial variability of mechanical properties across the landscape remains largely unknown and imperfectly constrained. However, the sensitivity to soil moisture and rupture scenario is consistent across shear strength variations, supporting our primary findings. A more detailed discussion on model assumptions and sensitivity analyses for RG3D is provided in Mathews et al. (2024).

5. Conclusions

We quantified the influence of seasonal and inter-seasonal soil moisture variability on coseismic shallow landslide initiation in the Oregon Coast Range under a range of Cascadia Subduction Zone rupture scenarios. Using a deterministic slope stability framework, we evaluated landslide area density (LAD), scaling relationships, and spatial distributions of yield acceleration while accounting for shear strength uncertainty.

Our results show that antecedent soil moisture is a primary control on coseismic landslide response. Wetter conditions reduce effective stress, increasing LAD and lowering yield accelerations. However, this sensitivity is diminished in winter months, when soils are persistently wet and additional variations in moisture have a relatively small effect on slope stability. These findings indicate that antecedent rainfall strongly preconditions hillslope stability and that earthquake magnitude alone does not determine regional-scale landslide response. Spatial analyses further reveal that landslide hazard is elevated in the western Coast Range, where high soil moisture coincides with strong seismicity, and that yield acceleration maps provide a direct link between earthquake shaking and landslide susceptibility

Overall, our results demonstrate that coseismic landslide initiation temporally dynamic and strongly dependent on seasonality and inter-seasonal wetness, highlighting that incorporating variable hydrological conditions into seismic landslide hazard assessments provides a more realistic representation of landscape response near the Cascadia Subduction Zone or in other seismically active regions.

Acknowledgements

Ben Leshchinsky and Michael Olsen acknowledge support under National Science Foundation (NSF) grant CMMI-2050047 and Oregon Department of Transportation research project SPR808. We acknowledge Kate Allstadt for constructive feedback that has improved the quality of this work.

Open Research

The source code for RegionGrow3D is available at https://doi.org/10.5066/P1BSMGGD (Mathews & Leshchinsky, 2024). Basemap in Figures 2a-b provided by OpenStreetMap (OpenStreetMap contributors, 2017; https://www.openstreetmap.org). Hillshade in Figures 2b, 4a, and 7a-c created using lidar from the Oregon Lidar Consortium (Oregon Department of Geology and Mineral Industries, 2022; https://www.oregon.gov/dogami/lidar/Pages/index.aspx). State boundary data in Figure 2a provided by the U.S. Census Bureau (U.S. Census Bureau, 2011; https://www.sciencebase.gov/catalog/item/52c78623e4b060b9ebca5be5). Highway network data in Figure 2b provided by the Oregon Department of Transportation (Oregon Department of Transportation, 2017; https://www.oregon.gov/odot/Data/Pages/GIS-Data.aspx). Soil texture data in Figure 2b determined using sand and clay content data from SoilGrids250m (Hengl et al., 2017; https://files.isric.org/soilgrids/former/2017-03-10/data/). Landslide polygons in Figure 2b are from

the Statewide Landslide Information Database for Oregon (SLIDO; Burns et al., 2012; Franczyk et al., 2019; https://www.oregon.gov/dogami/slido/Pages/data.aspx). Volumetric water content data in Figures 2c-d are from Soil Moisture Active Passive (SMAP; Reichle et al., 2019), accessed from https://appeears.earthdatacloud.nasa.gov/. Peak ground acceleration data in Figures 2e-f are from Sharifi-Mood (2017) and may be accessed through https://ohelp.oregonstate.edu/.

Statements and Declarations

Competing Interests:

The authors declare no competing interests.

References

Bayer, K. (2017, December 13). Quake-damaged SH1 north of Kaikoura to finally reopen after "unprecedented" 13 month repair job. *NZ Herald*. Retrieved from https://www.nzherald.co.nz/nz/quake-damaged-sh1-north-of-kaikoura-to-finally-reopen-after-unprecedented-13-month-repair-job/DYB5GJRSZSFKADWRMQCFXJVLLA/

Boore, D. M., & Atkinson, G. M. (2008). Ground-motion prediction equations for the average horizontal component of PGA, PGV, and 5%-damped PSA at spectral periods between 0.01 s and 10.0 s. *Earthquake Spectra*, *24*(1), 99–138. https://doi.org/10.1193/1.2830434

Bunn, M., Leshchinsky, B., & Olsen, M. J. (2020a). Estimates of three-dimensional rupture surface geometry of deep-seated landslides using landslide inventories and high-resolution topographic data. *Geomorphology*, *367*, 107332. https://doi.org/10.1016/j.geomorph.2020.107332

Bunn, M., Leshchinsky, B., & Olsen, M. J. (2020b). Geologic Trends in Shear Strength Properties Inferred Through Three-Dimensional Back Analysis of Landslide Inventories. *Journal of Geophysical Research: Earth Surface*, *125*(9). https://doi.org/10.1029/2019JF005461

Burns, W., Duplantis, S., Mickelson, K., Spritzer, J., & Wells, R. (2012). Landslide inventory maps of the Gales Creek quadrangle, Washington County, Oregon. *Oregon Department of Geology and Mineral Industries, Portland, Oregon, Interpretive Map Series-46, Scale*, *1*, 8000.

Dadson, S. J., Hovius, N., Chen, H., Dade, W. B., Lin, J.-C., Hsu, M.-L., et al. (2004). Earthquake-triggered increase in sediment delivery from an active mountain belt. *Geology*, *32*(8), 733. https://doi.org/10.1130/G20639.1

Froude, M. J., & Petley, D. N. (2018). Global fatal landslide occurrence from 2004 to 2016. *Natural Hazards and Earth System Sciences*, *18*(8), 2161–2181. https://doi.org/10.5194/nhess-18-2161-2018

van Genuchten, M. Th. (1980). A Closed-form Equation for Predicting the Hydraulic Conductivity of Unsaturated Soils. *Soil Science Society of America Journal*, *44*(5), 892–898. https://doi.org/10.2136/sssaj1980.03615995004400050002x

Goldfinger, C., Nelson, C., Morey, A., Johnson, J., Patton, J., Karabanov, E., et al. (2012). Turbidite event history—Methods and implications for Holocene paleoseismicity of the Cascadia subduction zone. *USGS Professional Paper*, *1661-F*, 184 pp.

Guzzetti, F., Ardizzone, F., Cardinali, M., Rossi, M., & Valigi, D. (2009). Landslide volumes and landslide mobilization rates in Umbria, central Italy. *Earth and Planetary Science Letters*, *279*(3–4), 222–229. https://doi.org/10.1016/j.epsl.2009.01.005

Hess, D. M., Leshchinsky, B. A., Bunn, M., Benjamin Mason, H., & Olsen, M. J. (2017). A simplified three-dimensional shallow landslide susceptibility framework considering topography and seismicity. *Landslides*, *14*(5), 1677–1697. https://doi.org/10.1007/s10346-017-0810-2

Huang, R., & Fan, X. (2013). The landslide story. *Nature Geoscience*, *6*(5), 325–326. https://doi.org/10.1038/ngeo1806

Jibson, R. W. (2011). Methods for assessing the stability of slopes during earthquakes—A retrospective. *Engineering Geology*, *122*(1–2), 43–50. https://doi.org/10.1016/j.enggeo.2010.09.017

Keefer, D. K. (1984). Landslides caused by earthquakes. *Geological Society of America Bulletin*, *95*(4), 406–421. https://doi.org/10.1130/0016-7606(1984)95<406:LCBE>2.0.CO;2

Keefer, D. K. (2002). Investigating Landslides Caused by Earthquakes – A Historical Review. *Surveys in Geophysics*, *23*(6), 473–510. https://doi.org/10.1023/A:1021274710840

Kramer, S. L. (1996). *Geotechnical earthquake engineering*. Pearson Education India.

Lehmann, P., von Ruette, J., & Or, D. (2019). Deforestation Effects on Rainfall-Induced Shallow Landslides: Remote Sensing and Physically-Based Modelling. *Water Resources Research*, *55*(11), 9962–9976. https://doi.org/10.1029/2019WR025233

Leshchinsky, B., Lehmann, P., & Or, D. (2021). Enhanced Rainfall-Induced Shallow Landslide Activity Following Seismic Disturbance—From Triggering to Healing. *Journal of Geophysical Research: Earth Surface*, *126*(1). https://doi.org/10.1029/2020JF005669

Lu, N., & Likos, W. J. (2006). Suction Stress Characteristic Curve for Unsaturated Soil. *Journal of Geotechnical and Geoenvironmental Engineering*, *132*(2), 131–142. https://doi.org/10.1061/(ASCE)1090-0241(2006)132:2(131)

Lu, N., & Likos, W. J. (2013). Origin of Cohesion and Its Dependence on Saturation for Granular Media. In *Poromechanics V* (pp. 1669–1675). Vienna, Austria: American Society of Civil Engineers. https://doi.org/10.1061/9780784412992.197

Madin, I., & Mabey, M. A. (1996). Earthquake hazard maps for Oregon. Department of Geology and Mineral Industries. Retrieved from https://pubs.oregon.gov/dogami/gms/GMS-100.pdf

Madin, I., Priest, G. R., Mabey, M., Malone, S., Yelin, T., & Meier, D. (1993). Scotts Mills earthquake—Western Oregon's wake-up call. *Oregon Geology*, *55*(3), 51–58.

Makdisi, F. I., & Seed, H. B. (1978). Simplified Procedure for Estimating Dam and Embankment Earthquake-Induced Deformations. *Journal of the Geotechnical Engineering Division*, *104*(7), 849–867. https://doi.org/10.1061/AJGEB6.0000668

Malamud, B. D., Turcotte, D. L., Guzzetti, F., & Reichenbach, P. (2004). Landslide inventories and their statistical properties. *Earth Surface Processes and Landforms*, *29*(6), 687–711. https://doi.org/10.1002/esp.1064

Martino, S., Marmoni, G. M., Fiorucci, M., Ceci, A. F., Discenza, M. E., Rouhi, J., & Tedoradze, D. (2022). Role of Antecedent Rainfall in the Earthquake-Triggered Shallow Landslides Involving Unsaturated Slope Covers. *Applied Sciences*, *12*(6), 2917. https://doi.org/10.3390/app12062917

Massey, C., Townsend, D., Rosser, B., Morgenstern, R., Jones, K., Lukovic, B., & Davidson, J. (2021). Version 2.0 of the landslide inventory for the Mw 7.8 14 November 2016, Kaikōura Earthquake [Data set]. Designsafe-CI. https://doi.org/10.17603/DS2-1FTV-HM22

Mathews, N., Leshchinsky, B. A., Olsen, M. J., & Klar, A. (2019). Spatial distribution of yield accelerations and permanent displacements: A diagnostic tool for assessing seismic slope stability. *Soil Dynamics and Earthquake Engineering*, *126*, 105811. https://doi.org/10.1016/j.soildyn.2019.105811

Mathews, N. W., & Leshchinsky, B. A. (2024). RegionGrow3D: A Software for Characterizing Discrete Three-Dimensional Landslide Source Areas on a Regional Scale (Version 1.0.0) [Software]. *U.S. Geological Survey Software Release*. https://doi.org/10.5066/P1BSMGGD

Mathews, N. W., Leshchinsky, B. A., Mirus, B. B., Olsen, M. J., & Booth, A. M. (2024). RegionGrow3D: A Deterministic Analysis for Characterizing Discrete Three-Dimensional Landslide Source

Areas on a Regional Scale. *Journal of Geophysical Research: Earth Surface*, *129*(9), e2024JF007815. https://doi.org/10.1029/2024JF007815

Medwedeff, W. G., Clark, M. K., Zekkos, D., & West, A. J. (2020). Characteristic landslide distributions: An investigation of landscape controls on landslide size. *Earth and Planetary Science Letters*, *539*, 116203. https://doi.org/10.1016/j.epsl.2020.116203

Olsen, M. J., Ashford, S. A., Mahlingam, R., Sharifi-Mood, M., & Gillins, D. T. (2015). *Impacts of potential seismic landslides on lifeline corridors*. Oregon. Dept. of Transportation. Research Section.

OpenStreetMap contributors. (2017). OpenStreetMap Basemap [Dataset]. Retrieved from https://www.openstreetmap.org

Oregon Department of Geology and Mineral Industries. (2022). Oregon Lidar Consortium [Dataset]. Retrieved from https://www.oregon.gov/dogami/lidar/Pages/index.aspx

Parker, R. N., Densmore, A. L., Rosser, N. J., de Michele, M., Li, Y., Huang, R., et al. (2011). Mass wasting triggered by the 2008 Wenchuan earthquake is greater than orogenic growth. *Nature Geoscience*, *4*(7), 449–452. https://doi.org/10.1038/ngeo1154

Petley, D. (2018). Landslides triggered by the 6th September 2018 Hokkaido earthquake. Retrieved July 27, 2022, from https://blogs.agu.org/landslideblog/2018/09/06/landslides-6th-september-2018-hokkaido-earthquake/

Quenzer, R., & Friesz, A. M. (2015). AppEEARS: simple and intuitive access to analysis ready data (Vol. 2015, pp. IN51B-1801). Presented at the AGU Fall Meeting Abstracts.

Reichle, R. H., Liu, Q., Koster, R. D., Crow, W. T., De Lannoy, G. J. M., Kimball, J. S., et al. (2019). Version 4 of the SMAP Level-4 Soil Moisture Algorithm and Data Product. *Journal of Advances in Modeling Earth Systems*, *11*(10), 3106–3130. https://doi.org/10.1029/2019MS001729

554 Roback, K., Clark, M. K., West, A. J., Zekkos, D., Li, G., Gallen, S. F., et al. (2018). The size, distribution,
555 and mobility of landslides caused by the 2015 Mw7. 8 Gorkha earthquake, Nepal.
556 *Geomorphology*, *301*, 121–138. https://doi.org/10.1016/j.geomorph.2017.01.030
557 Roering, J. J. (2008). How well can hillslope evolution models “explain” topography? Simulating soil
558 transport and production with high-resolution topographic data. *Geological Society of*
559 *America Bulletin*, *120*(9–10), 1248–1262. https://doi.org/10.1130/B26283.1
560 Sarma, S. K. (1973). Stability analysis of embankments and slopes. *Geotechnique*, *23*(3), 423–433.
561 https://doi.org/10.1680/geot.1973.23.3.423
562 Schaap, M. G., Leij, F. J., & van Genuchten, M. Th. (2001). ROSETTA: a computer program for
563 estimating soil hydraulic parameters with hierarchical pedotransfer functions. *Journal of*
564 *Hydrology*, *251*(3–4), 163–176. https://doi.org/10.1016/S0022-1694(01)00466-8
565 Schuster, R. L., & Highland, L. M. (2001). *Socioeconomic and environmental impacts of landslides in*
566 *the Western Hemisphere* (Report No. 2001–276). https://doi.org/10.3133/ofr01276
567 Sharifi-Mood, M. (2017). *Probabilistic geospatial analyses, uncertainty modeling, and mapping of*
568 *seismically-induced ground failures (Doctoral dissertation)* (Doctoral dissertation). Oregon
569 State University.
570 Smith, R., & Roe, W. (2015). Oregon geologic data compilation (OGDC)—Release 6. *Oregon*
571 *Department of Geology and Mineral Industries (DOGAMI), Open-File Rept. O-13*, *12*.
572 Terzaghi, K. (1950). Mechanism of Landslides. In S. Paige (Ed.), *Application of Geology to Engineering*
573 *Practice* (p. 0). Geological Society of America. https://doi.org/10.1130/Berkey.1950.83
574 Wang, F., Fan, X., Yunus, A. P., Siva Subramanian, S., Alonso-Rodriguez, A., Dai, L., et al. (2019).
575 Coseismic landslides triggered by the 2018 Hokkaido, Japan (Mw 6.6), earthquake: spatial
576 distribution, controlling factors, and possible failure mechanism. *Landslides*, *16*(8), 1551–
577 1566. https://doi.org/10.1007/s10346-019-01187-7

578 Wartman, J., Dunham, L., Tiwari, B., & Pradel, D. (2013). Landslides in Eastern Honshu Induced by
579 the 2011 Tohoku Earthquake. *Bulletin of the Seismological Society of America*, *103*(2B),
580 1503–1521. https://doi.org/10.1785/0120120128
581 Wieczorek, G. F. (1996). Landslides: investigation and mitigation. Chapter 4-Landslide triggering
582 mechanisms. *Transportation Research Board Special Report*, (247).
583 Wiley, T. J., Sherrod, D. R., Keefer, D. K., Qamar, A., Schuster, R. L., Dewey, J. W., et al. (1993).
584 Klamath Falls earthquakes, September 20, 1993—including the strongest quake ever
585 measured in Oregon. *Oregon Geology*, *55*(6), 127–134.
586 Worden, C. B., Hearne, M., & Thompson, E. M. (2018). ShakeMap v4 Software. *USGS Software*
587 *Release*. Retrieved from https://doi.org/10.5066/P97FHE0I
588 Zhang, S., & Wang, F. (2019). Three-dimensional seismic slope stability assessment with the
589 application of Scoops3D and GIS: a case study in Atsuma, Hokkaido. *Geoenvironmental*
590 *Disasters*, *6*(1), 9. https://doi.org/10.1186/s40677-019-0125-9
591 Zhang, S., Li, R., Wang, F., & Iio, A. (2019). Characteristics of landslides triggered by the 2018
592 Hokkaido Eastern Iburi earthquake, Northern Japan. *Landslides*, *16*(9), 1691–1708.
593 https://doi.org/10.1007/s10346-019-01207-6
594

Supplementary Files

This is a list of supplementary files associated with this preprint. Click to download.

- coseismiclandslidesandsoilmoistureSInathaz.docx